A laboratory model for a meandering zonal jet

K.D. Stewart[1], **F. Macleod**[1]

[1]Research School of Earth Sciences, Australian National University, Canberra, Australia

Key Points:

- We use a novel laboratory experiment to investigate zonal jet dynamics and distinguish between standing meanders and transient eddies.
- Flows occupy two distinct regimes; predominantly zonal, or predominantly meandering, depending on the timescales of forcing and dissipation.
- For predominantly meandering flow, the standing meanders perform 81±14% of meridional tracer transport, with 15±16% by transient eddies.

Corresponding author: K.D. Stewart, kial.stewart@anu.edu.au

Abstract

The meandering jet streams of the Northern Hemisphere influence the weather for more than half of Earth's population, so it is imperative that we improve our understanding of their behaviour and how they might respond to climate change. Here we describe a novel laboratory model for a meandering zonal jet. This model comprises a large rotating annulus with a series of topographic ridges, and an imposed radial vorticity flux. Flow interactions with the topographic ridges operate to concentrate the zonal transport into a narrow jet, which supports the development and propagation of Rossby waves. We investigate the dynamics of the jet for a range of rotation rates, imposed radial vorticity fluxes, and topographic ridge configurations. The circulations are classified into two distinct regimes: predominantly zonal, or predominantly meandering. The flow regime can be quantified by the ratio of the Ekman dissipation and jet advection timescales, which gives an indication of whether disturbances arising from the flow-topography interaction are dissipated faster than the time taken to circuit the annulus; if not, these disturbances will re-encounter the topography, and thus be reinforced and amplified. For predominantly zonal flows, the radial vorticity flux is mainly performed by transient eddies. For predominantly meandering flows, standing meanders perform 81±14% of the radial vorticity flux, with 15±16% accommodated by the transient eddies. Our experiments indicate that the Arctic amplification associated with climate change will tend to favour predominantly zonal flow conditions, suggesting a reduced occurrence of atmospheric blocking events caused by the jet streams.

Plain Language Summary

Jet streams are narrow, meandering bands of intense eastward winds circling Earth in the upper atmosphere. They are a prominent dynamical feature of Earth's climate system and have major implications for navigation and weather prediction. Modelling the jet streams is important for understanding their dynamics and how they might be affected by climate change. Here we describe a new approach for laboratory experiments to model meandering jets like the jet streams. The laboratory circulations can be classified into two distinct flow states; one which is predominantly eastward, or one which has substantial north-south meanders in addition to its eastward flow. The flow state of a particular experiment is shown to depend on the relative strength of the forcing and the rate at which the jet variability is dissipated.

1 Introduction

Zonal jets have a leading-order influence on Earth's atmosphere and weather (Galperin & Read, 2019). Their dynamics are associated with many occurrences of synoptic variability, including persistent and extreme weather events. Central to their existence is the β-effect, arising from the latitudinal variation of the Coriolis parameter, which leads to the zonalisation of motions and promotes an inverse cascade of energy from geostrophic turbulence to zonal flows of relatively larger lengthscales (e.g., Rhines, 1975). Projected changes to the atmospheric conditions driving zonal jets will likely have consequences for jet behaviour, although the exact nature of these consequences remains uncertain (e.g., Francis & Vavrus, 2012; Hassanzedeh et al., 2014; Hoskins & Woollings, 2015). Therefore, it is important to improve the understanding of the response of zonal jet dynamics to changes in the atmospheric state.

One characteristic dynamic of zonal jets are the planetary Rossby waves that appear as meridional meanders of the jet core with latitudinal excursions of relatively cold and warm air masses (e.g. Rhines, 1975). The westward propagation of these Rossby waves opposes the eastward flowing polar and subtropical jets, meaning the meridional meanders drift eastwards relatively slower than the host jets, prolonging the presence of the

associated anomalous air masses. Under certain atmospheric forcing, the zonal propagations of the Rossby waves and zonal jets can cancel one another, leading to a state of stationary, amplified meridional meanders with persistent anomalous weather conditions (e.g., Hoskins et al., 1985). This particular state of the zonal jet is referred to as a "blocked" flow regime, which, when compared to the typical "zonal" flow regime, is associated with a persistent obstruction to the zonal flow, enhanced meridional flows, anticyclonic circulation at high latitudes, and cyclonic circulation at low latitudes (e.g., Woollings et al., 2018). As such, local synoptic variability tends to be damped during periods of blocked flow, leading to prolonged and often extreme weather conditions.

Numerical climate and atmospheric models are key to developing our understanding of zonal jet behaviour and how it might be affected by climate change. However, insights from numerical simulations must be interpreted while cognisant of individual model biases, simplifying assumptions inherent to the simulation, and subjective decisions concerning resolution and parameterisations. The wide range of time and spatial scales spanned by zonal jet dynamics means their representation in numerical simulations are particularly sensitive to model resolution, with insufficient resolution tending to under estimate the crucial eddy–mean flow interactions and bias the zonal jet locations equatorward (e.g., Lu et al., 2015). Performing numerical simulations at the high resolutions necessary to achieve geophysically relevant and informative zonal jet behaviour is computationally expensive and can limit the range of parameter space able to be explored. With this in mind, it can be useful to complement numerical investigations of zonal jets with alternative approaches.

Laboratory experiments with homogenous rotating fluids are a powerful means of examining zonal jet dynamics (Read, 2019). In such experiments, the important β-effect is emulated topographically by a gradient in the depth of the working fluid, which is achieved by incorporating a sloping tank base and/or the parabolic free surface of fluid in solid body rotation. The methodologies to generate the barotropic zonal jet flows in the laboratory can be broadly classified into two mechanisms; directly- and indirectly-forced jets. For the first class, the directly-forced zonal jets can be shear-driven by differentially moving boundaries (e.g., Hide & Titman, 1967; Aguiar et al., 2010), or result from the conservation of angular momentum and an imposed radial flow between sources and sinks at different radii (e.g., Hide, 1968; Sommeria et al., 1989; Solomon et al., 1993; Weeks et al., 1997; Tian et al., 2001). Indirectly-forced jets are the product of nonlinear eddy dynamics; active forcing generates and maintains an eddy field characterised by relatively small lengthscales, which becomes anisotropic due to the β-effect and cascades energy into larger-scale zonal flows, and ultimately, an eddy-driven zonal jet (e.g., Cabanes et al., 2017; Lemasquerier et al., 2021). While indirectly-forced eddy-driven jets represent the fundamental case where jet dynamics are decoupled from the specifics of the forcing configuration, they are challenging to generate in the laboratory because substantial zonalisation of flows requires a strong β-effect.

Experiments with directly-forced zonal jets provide an effective, controllable and repeatable technique to investigate jet dynamics and their response to changing forcing conditions. The case of zonal jets driven by shear from a moving boundary, such as a differentially-rotating surface in contact with the fluid, are relatively simple to construct and observe (e.g., Niino & Masawa, 1984; Früh & Read, 1999; Aguiar et al., 2010). However, as the strength of the shear forcing intensifies, the lengthscales of the excited flows reduces and the radial extent of the jet becomes tightly confined to the regions of the forcing, eventually resembling a series of small-scale vortices rather than a zonal jet (Read et al., 2020). Zonal jets driven by an imposed radial flow are also sensitive to the radial distribution of the forcing; theoretical predictions and observations of the average zonal velocity profile indicate the zonal flow to be confined between the source and sink radii (Hide, 1968; Solomon et al., 1993). Indeed, numerical simulations designed to model laboratory experiments demonstrate that the discontinuities of potential vorticity associ-

ated with the forcing configuration tend to lie either side of the jet, and thereby influence the jet behaviour (Marcus & Lee, 1998). Thus, while directly-forced zonal jets are a convenient method of examine jet behaviour in the laboratory, the radial constraints imposed by the forcing configurations mean that some geophysically-relevant elements of the zonal jet dynamics can be suppressed, such as the uninhibited development of meridional meanders, or details of the across-jet fluxes.

The imposed radial flow methodology for generating directly-forced zonal jets of Sommeria et al. (1989) and Solomon et al. (1993) has been used by Weeks et al. (1997) and Tian et al. (2001) to investigate the effect of zonally-varying bottom topography on the circulation. In these experiments, the bottom topography consisted of broad, small-amplitude, symmetric rigid mountains of zonal wavenumber-2, which are the laboratory analogue of the North American and Eurasian continents. The forcing is characterised by a non-dimensional Rossby number based on the tank rotation rate and imposed radial flow (where a low Rossby number implies a lower imposed radial flow and/or higher tank rotation rate). Weeks et al. (1997) and Tian et al. (2001) achieved persistent flow states reminiscent of the "blocked" and "zonal" flow regimes for low and high Rossby numbers, respectively, with intermediate forcing conditions leading to intermittent flow regime that spontaneously switched between the blocked and zonal flow states. Both the blocked and zonal flow regimes exhibited a strong imprint of the topographic wavenumber-2, with their phases zonally-fixed relative to the topography; the blocked flow regime also featured the harmonic of zonal wavenumber-4. The dominance of these low wavenumber structures is indicative of the governing role that the wavenumber-2 topography is playing in setting the circulation, and raises the question of whether the flow state itself is sensitive to the specifics of the topography.

Here we describe laboratory experiments with a barotropic zonal jet performed in a rotating annulus with a radially-sloping bottom, imposed radial flow, and a series of localised topographic ridges. The imposed radial flow enters the annulus at the outer edge wall and drains over the inner edge wall, thereby spanning the entire width of the annulus; the dynamical implication of this flow is that it serves as an imposed radial vorticity flux. A set of three localised topographic ridges span a quarter of the annular circumference and the inner third of the annular radius; these ridges act to interrupt the zonal flow as it nears the inner edge wall, giving rise to radial structure in the average zonal velocity that consists of a mid-annulus maximum. One of these inner ridges is able to be extended radially to occupy a greater fraction of the annular radius. The interaction between zonal circulation arising from the imposed radial flow and the topographic ridges generates a coherent zonal jet. In this approach, the flow-topography interaction sets the radial position and phase of the zonal jet at the location of the topography; the jet is subsequently free to evolve downstream as dynamics require. We investigate the influences of the tank rotation rate, imposed radial flow, and radial extent of the ridge on the flow state and the zonal jet dynamics, with a focus on the role of the jet meanders in accommodating the imposed radial flow.

The layout of the paper is as follows. In §2 we introduce theoretical considerations important to our analysis. In §3 we describe the laboratory apparatus, methodology and analysis. In §4 we present and discuss the results of the experiments. We provide a brief commentary on the geophysical implications of our results in §5, and our conclusions in §6.

2 Theoretical Background

We consider the circulation dynamics of a homogenous fluid in an annulus that has outer and inner edge radii r_o and r_i, respectively (Fig. 1). The outer and inner edge wall heights, H_o and H_i respectively, with $H_o > H_i$; this means that when the annulus is completely full, any additional fluid added to the annulus causes an equal volume of fluid

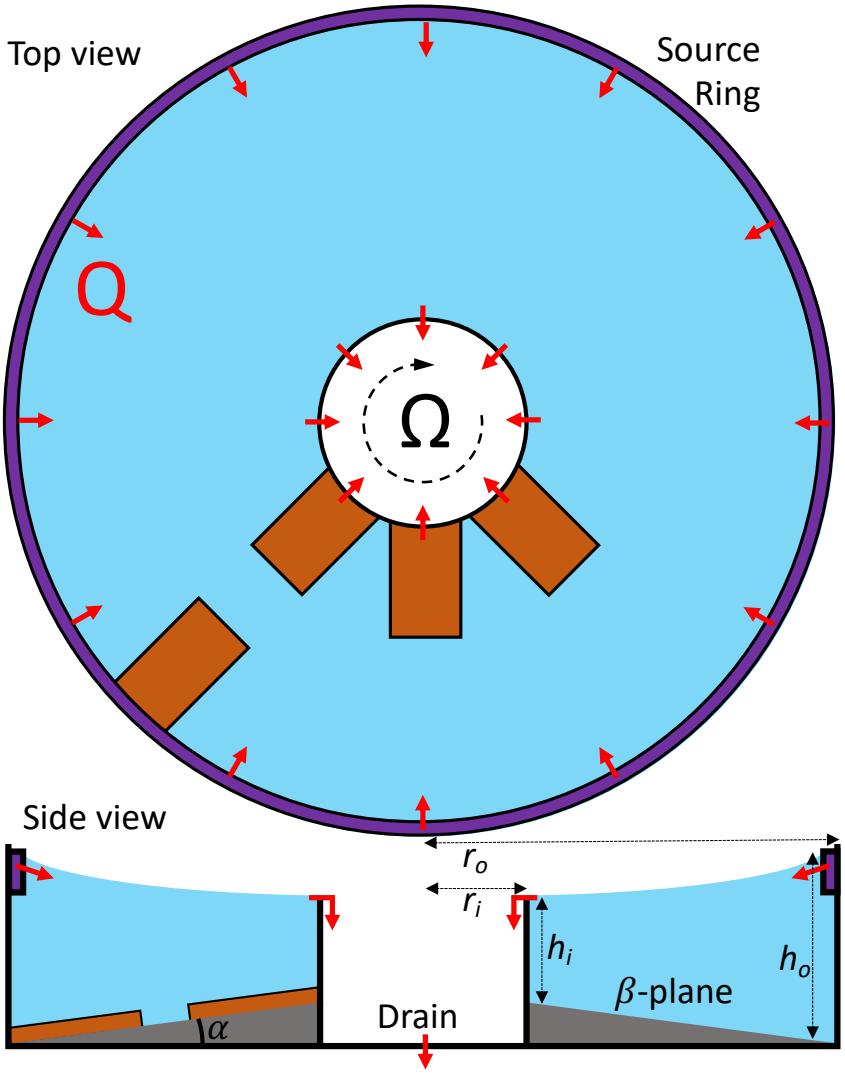

Figure 1. A schematic depicting the geometry of the annulus rotating about the vertical axis at rate Ω. The imposed volume flux Q enters the annulus via the source ring at the outer edge wall (radius r_o) and overflows the inner edge wall (radius r_i). The base of the annulus is radially sloped at an angle α, and the free surface of the rotating fluid is quadratic in radius, such that the depth of the fluid decreases towards the inner edge wall. Four topographic ridges are permanently located on the sloping base; three against the inner edge wall and one against the outer edge wall. The gap between the outer and corresponding inner ridge is systematically varied.

to be displaced over the inner edge wall. The base of the annulus is sloped at an angle α in the radial direction such that when the annulus and fluid are at rest in the inertial frame, the depth of the fluid at rest h_r increases linearly with radius r from $h_r(r_i) = h_i$ as,

$$h_r(r) = h_i + (r - r_i)\tan\alpha. \tag{1}$$

The annulus of fluid rotates about its central vertical axis at a steady rate of Ω (rad/s). This background rotation, and the subsequent balance between the hydrostatic pressure and centrifugal acceleration of the fluid, causes the free surface height of the fluid to obtain a parabolic shape that is dependent on the radius squared. That is, when the annulus is completely full of fluid and in solid body rotation at Ω, the depth of the fluid is,

$$h(r) = h_i + (r - r_i)\tan\alpha + \frac{\Omega^2}{2g}\left(r^2 - r_i^2\right), \tag{2}$$

where g is gravity. The maximum water depth h_o occurs at the outer edge wall,

$$h(r_o) = h_o = h_i + (r_o - r_i)\tan\alpha + \frac{\Omega^2}{2g}\left(r_o^2 - r_i^2\right). \tag{3}$$

The total volume of the water in the rotating annulus is therefore a function of the rotation rate;

$$V(\Omega) = 2\pi\left(\frac{\Omega^2}{8g}\left(r_o^4 - r_i^4\right) + (h_o - h_i)\frac{\left(r_o^3 - r_i^3\right)}{3\left(r_o - r_i\right)} - \frac{\Omega^2 r_i^2}{4g}\left(r_o^2 - r_i^2\right) - \frac{r_i\left(h_o - h_i\right)}{2\left(r_o - r_i\right)}\left(r_o^2 - r_i^2\right) + \frac{h_i}{2}\left(r_o^2 - r_i^2\right)\right). \tag{4}$$

A steady volume flux Q (m^3/s) is imposed uniformly around the outer edge wall, causing an equal volume flux Q to be displaced from the annulus over the inner edge wall. This volume flux Q from the outer edge wall to the inner edge wall requires an average radial velocity $v(r)$,

$$v(r) = \frac{Q}{2\pi r h(r)}, \tag{5}$$

across the annulus.

If we assume that potential vorticity is conserved as the fluid flows across the annulus, and that the fluid enters the annulus with zero relative vorticity ζ (where $\zeta(r_o) = 0$), we can derive an expression for the relative vorticity as a function of radius. That is,

$$\frac{2\Omega + \zeta(r_o)}{h(r_o)} = \frac{2\Omega}{h_o} = \frac{2\Omega + \zeta(r)}{h(r)} \quad \rightarrow \quad \zeta(r) = 2\Omega\left(\frac{h(r)}{h_o} - 1\right). \tag{6}$$

The product of the above estimates for the imposed radial velocity (Eq. 5) and imposed relative vorticity (Eq. 6) provides an expression for the imposed radial vorticity flux $v\zeta$ as a function of radius,

$$v\zeta(r) = \frac{Q\Omega}{\pi r h(r)}\left(\frac{h(r)}{h_o} - 1\right). \tag{7}$$

This imposed radial vorticity flux is accommodated by the circulation dynamics of the fluid in the annulus.

Momentum dissipation by viscosity occurs in the lower Ekman boundary layer, which has thickness δ_{Ek} given by,

$$\delta_{Ek} = \sqrt{\frac{\nu}{\Omega}}, \tag{8}$$

where ν (m^2/s) is the kinematic viscosity of the fluid. From Holton and Hakim (2013), the conservation of potential vorticity in a barotropic fluid with a no-slip boundary condition allows temporal variations of the relative vorticity to be related to the vertical velocity at Ekman boundary layer, which subsequently provides a characteristic timescale τ_{Ek} for viscous flow dissipation within the Ekman layer,

$$\tau_{Ek} = \frac{h(r)}{\sqrt{\nu\Omega}}. \tag{9}$$

That is, τ_{Ek} is the time taken for relative vorticity to decrease to e^{-1} of its original value, and is often referred to as the barotropic spin-down timescale. Here, Ekman dissipation is the dominant mechanism that damps flow at all scales, including eddies and small-scale flow variability.

Hide (1968) provides a theoretical prediction for the zonal velocity in a rotating annulus with radially separated sources and sinks:

$$u(r) = \frac{Q}{2\pi r}\sqrt{\frac{\Omega}{\nu}} = \frac{Q}{2\pi r \delta_{Ek}}, \tag{10}$$

which, interestingly, depends on the thickness of the Ekman layer, and not the total fluid depth; the laboratory experiments of (Solomon et al., 1993) report good agreement between their measurements and this predicted zonal velocity profile. The predicted zonal velocity allows us to define a zonal advection timescale τ_{adv} as the time taken to circuit the annulus,

$$\tau_{adv}(r) = \frac{2\pi r}{u(r)} = \frac{4\pi^2 r^2 \delta_{Ek}}{Q}. \tag{11}$$

The zonal advection timescale can be used with the Ekman dissipation timescale to give the ratio,

$$\frac{\tau_{Ek}}{\tau_{adv}(r)} = \frac{Qh(r)}{4\pi^2 r^2 \nu}, \tag{12}$$

which offers an indication of the dynamical longevity of variability in the flow; that is, whether eddies are damped faster than the time taken for them to be advected around the annulus. Note that this timescale ratio is independent of the rotation rate Ω.

The total zonal and radial velocities, (u, v) respectively, can each be decomposed into three contributing terms; $(\overline{u}, \overline{v})$, which are the time-mean–zonal-mean velocities, $(\hat{u}, \hat{v})$, which are the time-mean of the deviations from the zonal-mean velocities, and (u', v'), which are the time-dependent deviations from the zonal-mean velocities. That is,

$$u(r,\theta,t) = \overline{u}(r) + \hat{u}(r,\theta) + u'(r,\theta,t) \quad \text{and} \quad v(r,\theta,t) = \overline{v}(r) + \hat{v}(r,\theta) + v'(r,\theta,t). \tag{13}$$

These three terms are referred to as the time-mean–zonal-mean flow, the standing meanders, and the transient eddies, respectively. Hereafter, in the interests of lucidity, subsequent equations will no longer include the dependencies of their terms.

The time-means of the transient eddies are zero, so the time-means of the total velocities are simply the time-mean–zonal-mean flows plus the standing meanders,

$$\langle u \rangle = \overline{u} + \hat{u} \quad \text{and} \quad \langle v \rangle = \overline{v} + \hat{v}, \tag{14}$$

where the angled brackets $\langle . \rangle$ are used to denote time-means.

As the time-mean of the transient eddies is zero, in order to compare the relative magnitudes of the transient eddies with the other velocity components, it is convenient to use the time-mean of Equation (13) squared; that is,

$$u^2 = \left(\overline{u} + \hat{u} + u'\right)^2 = \overline{u}^2 + 2\overline{u}\hat{u} + 2\overline{u}u' + \hat{u}^2 + 2\hat{u}u' + u'^2 \tag{15}$$

$$\left\langle u^2 \right\rangle = \left\langle \overline{u}^2 \right\rangle + \left\langle 2\overline{u}\hat{u} \right\rangle + \left\langle \hat{u}^2 \right\rangle + \left\langle u'^2 \right\rangle \quad \rightarrow \quad \left\langle u'^2 \right\rangle = \left\langle u^2 \right\rangle - \overline{u}^2 - 2\overline{u}\hat{u} - \hat{u}^2, \tag{16}$$

which allows us to compare $\overline{u}$, $\hat{u}$ and $\sqrt{\left\langle u'^2 \right\rangle}$ as the zonal velocity components of the time-mean–zonal-mean flow, the standing meanders, and the transient eddies, respectively, and similarly for the radial velocity v.

The relative vorticity ζ can also be decomposed in a similar manner,

$$\zeta = \overline{\zeta} + \hat{\zeta} + \zeta'. \tag{17}$$

The time-mean radial vorticity flux $\langle v\zeta \rangle$ can be expressed as the time-mean of the product of Equations (13) and (17),

$$\langle v\zeta \rangle = \left\langle (\overline{v} + \hat{v} + v') \left(\overline{\zeta} + \hat{\zeta} + \zeta' \right) \right\rangle = \overline{v} \left(\overline{\zeta} + \hat{\zeta} \right) + \hat{v} \left(\overline{\zeta} + \hat{\zeta} \right) + \langle v'\zeta' \rangle \,, \tag{18}$$

where the three terms of the righthand side describe the radial vorticity flux contributions by the time-mean–zonal-mean flow, standing meanders, and transient eddies, respectively. In practice, the cross terms $\overline{v}\hat{\zeta}$ and $\overline{\zeta}\hat{v}$ are negligible and zonally-average to zero, so we focus our analysis on the $\overline{v}\overline{\zeta}$, $\hat{v}\hat{\zeta}$, and $\langle v'\zeta' \rangle$ terms as the time-mean–zonal-mean flow, standing meander, and transient eddy contributions of the radial vorticity flux:

$$\langle v\zeta \rangle = \overline{v}\overline{\zeta} + \hat{v}\hat{\zeta} + \langle v'\zeta' \rangle \,. \tag{19}$$

Here, the circulation in a rotating annulus is measured and compared with the theoretical predictions above. The observed flows are decomposed into their time-mean–zonal-mean, standing meanders, and transient eddy components, and the radial vorticity fluxes of each component is calculated.

3 Experiments

3.1 Laboratory Apparatus

We use the Large Rotating Annulus (LRA) facility in the Geophysical Fluid Dynamics Laboratory at the Australian National University (Fig. 2). The LRA facility consists of a perspex tank with a 0.4 m high outer edge wall at radius $r_o = 0.8$ m, filled with a working fluid and mounted centrally on a table that is able to be rotated at a precise rate; here we use three clockwise rotation rates of $\Omega = (0.5,\, 1.0,\, 1.5)\ \pm 10^{-4}$ rad/s. The outer edge wall is completely surrounded by an isolated, water-filled chamber that serves both structural and insulation purposes. The LRA has a modular central section that allows the specifics of the inner edge wall to be varied as required. In the configuration employed here, the inner edge wall is 0.2 m high (measured from the flat base of the LRA) and at a radius $r_i = 0.2$ m. A 1.6 m diameter truncated cone machined from a single block of perspex is fixed to the flat base of the LRA; this false floor has large and small radii of r_o and r_i, respectively, and a maximum height of 0.05 m (such that the functional depth of the working fluid at the inner edge wall is $h_i = 0.15$ m). The LRA has 4 independent fluid couplings that provide plumbed lines between the laboratory and rotating table. Two Teradek systems mounted on the LRA allow for high bandwidth digital signals to be wirelessly broadcast from the LRA to the laboratory. The temperature of the LRA, working fluid, and laboratory are all held constant at 20±0.5°C.

A ring of 13 mm diameter hose with regular 0.5 mm perforations every 100 mm is located at the outer edge wall, and serves as the source of the imposed volume flux Q of working fluid. This ring is held in place by a tensioned perspex sleeve and a two strips of 50×20 mm porous sponge foam, one above and one below the hose. The sponge layer acts to remove any momentum associated with the imposed volume flux as it enters the annulus, and to even out the flow to ensure a zonally-uniform distribution. When the

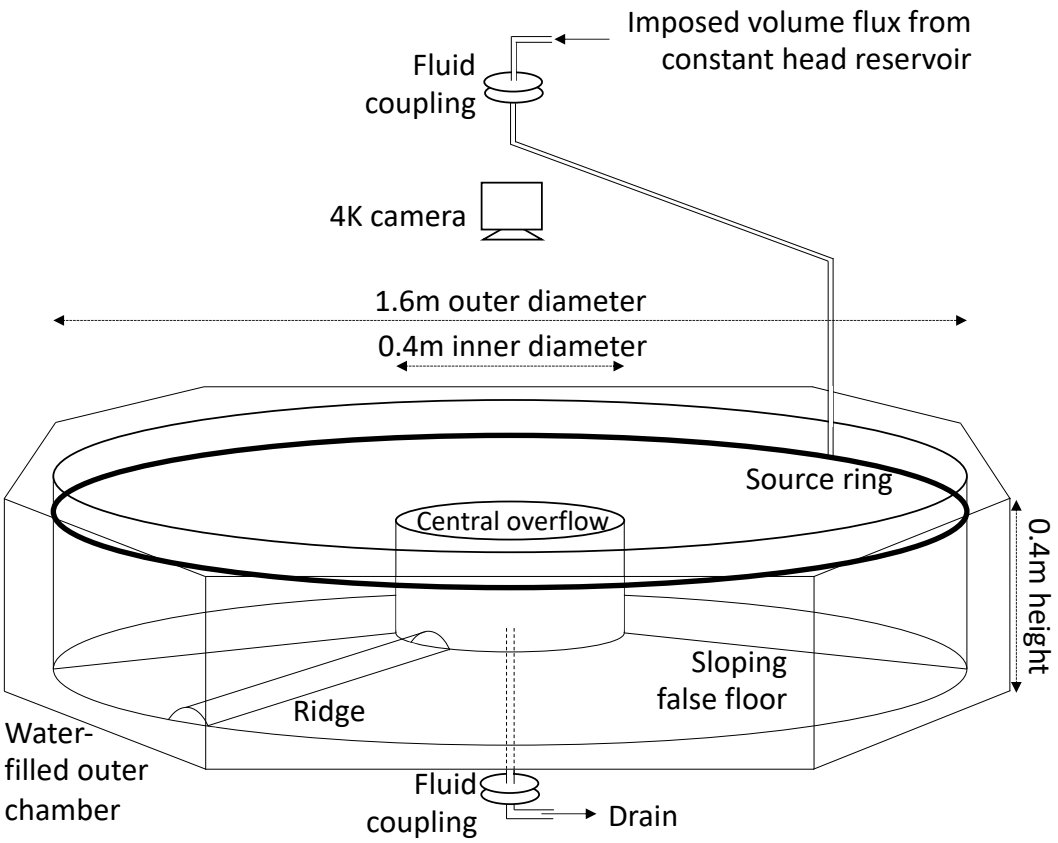

Figure 2. A schematic depicting elements of the Large Rotating Annulus (LRA) tank facility at the Australian National University. The tank, camera, and fluid couplings are mounted on a table able to be rotated at a precise rate. Note that the inner ridges are not shown here.

annulus is completely full, the imposed volume flux Q is accommodated by an overflow of working fluid over the inner edge wall. A thin strip of cotton material is fixed to the upper rim of the inner edge wall to ensure zonally-uniform drainage by breaking the surface tension of the overflow.

The working fluid is a brine made from tap water and sodium chloride with a density of $1025 < \rho < 1028\,\mathrm{kg/m^3}$, which was needed in order to be slightly denser than the small suspended Pliolite particles used for flow visualisation. This working fluid is prepared in advance in a separate, continuously-mixed 2200 L reservoir and allowed to thermally equilibrate with the laboratory. The working fluid is pumped from the large reservoir up to a constant head bucket, which overflows back to the reservoir. 2 of the LRA's 4 fluid couplings are employed in this configuration; the first is used to impose the steady volume flux Q through the ring at the outer edge wall, and the second as a central drain of the water overflowing the inner edge wall. The imposed volume flux is set by adjusting the opening of a valve between the constant head bucket of working fluid and the LRA. The imposed volume flux Q is quantified by measuring the ∼10 minute average flow rate of the working fluid as it drains off the LRA. Here we imposed 6 different volume fluxes spanning Q =11–98 mL/s.

Cylindrical segments representative of topographic ridges were placed on the sloping false floor to generate localised structure in the flow. These ridges had a zonal extent of 100 mm with a maximum height of 40 mm above the sloping false floor. Three of the ridges were permanently located against the inner edge wall; these inner ridges were all radially 200 mm wide and positioned in series to span a quarter of the zonal circumference. These inner ridges remained in place for all experiments and acted to slow the flow around the annulus at small radii. A fourth 200 mm wide ridge was permanently located against the outer edge wall and radially aligned with the permanent inner ridge that was most clockwise. The configuration of these permanent ridges amounts to 1/3 of the annular radial width remaining open; auxiliary experiments with larger sections remaining open (by shortening the radial extent of the outer ridge) indicated no qualitative difference from this 1/3 configuration. An additional three ridges were separately placed in the radial gap between the aligned outer and inner ridges against the inner ridge providing three additional ridge configurations. These three additional ridges were 100 mm, 150 mm and 200 mm wide; the first two amount to radial gaps or openings of 1/6 and 1/12 of the annular width, respectively, with the third ridge completely closing the gap. Recall that the false floor slopes 50 mm across the 600 mm radius of the annulus, meaning that for a completely closed ridge only the inner 120 mm of the annulus have continuous topographic contours around the annulus, and that these contours have a radial extent of 480 mm across the ridge (less when including the effect of the parabolic free surface). That is to say that the 40 mm high ridges impose a substantial dynamical barrier to the circulation. In summary, there are 4 ridge configurations; three with ridge gaps of 1/3, 1/6 and 1/12 the annular width, and one with no gap.

The flow is observed with a Sony Alpha 7 ii camera centrally-mounted on the LRA approximately 3 m above the free surface of the working fluid. The fixed length camera lens is selected so as to provide a view of the full annulus. The 4K resolution live signal from the camera is broadcast in real time by one of the Teradek systems to a computer server for immediate storage and subsequent analysis.

A pair of LED light strips are attached around the outer edge of the LRA and provide a near-uniform illumination throughout the annulus. Passive Pliolite tracer particles of diameter 400–600μm and density $\sim$ 1022kg/m^3 are presoaked in an ultrasonic bath with a wetting agent and distributed throughout the working fluid to visualise the flow. The small density difference between the Pliolite and slightly denser working fluid ensures that the particles tend to stay in the upper regions of the working fluid and remain above the Ekman layer at the base of the annulus. The top sides of the truncated

cone false floor and topographic ridges are painted black to maximise the contrast between them and the white Pliolite particles.

3.2 Methodology

The 2200 L reservoir is filled with water and sufficient salt to produce the brine at the desired density; this brine is continuously mixed and allowed to thermally equilibrate to the laboratory temperature (at least 24 hours). Once the brine has equilibrated, the stationary annulus is filled the brine solution via a rapid pump system (approximately 350 L in 15 minutes). During this time the topographic ridge configuration is set, LED light strips are turned on, and a sample of the brine and wetting agent are used to presoak the Pliolite particles in an ultrasonic bath. When the annulus is full, the rapid pump system is removed and the imposed flow rate Q is activated. The LRA is then set to rotate at the desired rate Ω and allowed to spin up to a statistically equilibrated state.

A substantial portion of the spin up timescale includes filling of the volumetric adjustment. That is, the total volume of working fluid able to be accommodated in the full annulus at rest is less than that once the LRA is spinning. This timescale can be estimated analytically by calculating the difference between the total volume of the full annulus for a given rotation rate and the total volume at rest (via Eq. 4), and dividing this by the imposed volume flux Q. It can also be measured by quantifying the flow rate of the fluid overflowing the inner edge wall, which is monitored throughout the course of each experiment. The upper end member of this timescale is the case with the fastest rotation rate and smallest imposed volume flux, returning a volumetric adjustment timescale of $\sim 4 \times 10^3$ seconds. Following this volumetric adjustment timescale, the circulation undergoes a dynamical adjustment towards statistical equilibrium, which we observe to be approximately 30 minutes. As a conservative approach, we allow each experiment at least 2 hours of volumetric and dynamical adjustments before recording flow measurements.

Once we are satisfied with the dynamical state of the flow, approximately 30 mL of the soaked Pliolite solution is gently seeded into the working fluid via a large bore syringe. The circulation dynamics, which are minimally affected by the injection of the Pliolite, act to further distribute the particles throughout the annulus, a process that that occurs within approximately 5 minutes.

When the particles are sufficiently distributed throughout the domain, the circulation is filmed in 4K resolution at 25 frames per second for at least 10 minutes. This footage is wirelessly broadcast in real time to a laboratory computer where it is saved to a server for later analysis.

Once the footage has been captured, the topographic ridges are adjusted to one of the three other configurations. This is a manual procedure that occurs without changing the rotation rate or imposed volume flux. As such, it does introduce substantial disturbances to the flow that must be allowed to settle. The settling timescale of the flow following the topographic reconfiguration is on the order of 10 minutes; as a conservative approach we allow the system at least 30 minutes to adjust to the new topographic configuration. Note that the sequence of topographic configurations varies between experiment sets, and the flow disturbance during the reconfiguration is substantial, so that the flow of a given topographic configuration is completely independent of the flow of the previous configuration.

When the flow has readjusted to the new topographic configuration, the Pliolite is reseeded throughout the working fluid and redistributed by the circulation, and footage of the flow captured again. This process is repeated for the 4 topographic configurations without adjusting the rotation rate Ω or imposed volume flux Q. The total time for this process is on the order of 5 hours for each pairing of rotation rate and imposed volume

flux. The total volume flux for this process is between approximately 200 L and 1800 L depending on the imposed volume flux Q. This rate of usage means that for experiments with lower values of Q we have sufficient brine remaining in the 2200 L reservoir such that we are able to simply change the rotation rate Ω and/or Q and continue running with the brine already in the annulus. For the larger values of Q, however, we must empty the annulus of the old brine and refill the reservoir with new brine for each experiment.

Table 1. A table of the parameter space explored by the 72 experiments. The rows are grouped by the three rotation rates Ω, and the columns by the four ridge gap configurations; the measured values of imposed volume flux Q are listed in mL/s.

Ω	Ridge Gap			
(rad/s)	1/3	1/6	1/12	0
0.5	14	11	14	17
0.5	39	39	37	37
0.5	50	49	48	48
0.5	67	66	67	67
0.5	80	82	81	82
0.5	95	95	95	94
1.0	15	13	13	14
1.0	38	38	37	38
1.0	50	49	49	48
1.0	64	66	65	65
1.0	81	82	80	84
1.0	97	97	97	97
1.5	18	19	18	19
1.5	33	32	30	31
1.5	44	47	45	48
1.5	63	60	64	63
1.5	80	83	80	83
1.5	98	96	94	94

3.3 Analysis

The ∼10 minutes of high resolution footage from each experiment were initially inspected to identify a single 200 second section that is both visually representative of the circulation dynamics and of optimal particle coverage. These 200 second sections were then parsed into 25 frame per second image sequences for each experiment. The images were subsequently cropped square to a 1054×1054 pixel region of interest, and masked to remove any signals outside of the annulus. Auxiliary testing with sections of longer durations was found to not substantially influence the following analysis.

Each set of images is analysed with OpenPIV, an open source Particle Image Velocimetry (PIV) Python package. Interrogation windows of size 16×16 pixels return timeseries of Eulerian velocities on a 70×70 grid with spatial resolution of 22 mm. These velocity fields are initially in the Cartesian reference frame of the camera before being transformed into timeseries of the zonal and radial velocities (u, v) in the reference frame of the rotating annulus, and used to calculate the relative vorticity ζ as the curl of the velocity field. These timeseries of zonal and radial velocities and relative vorticity are then decomposed into their respective time-mean–zonal-mean, standing meanders, and transient eddy components as per §2.

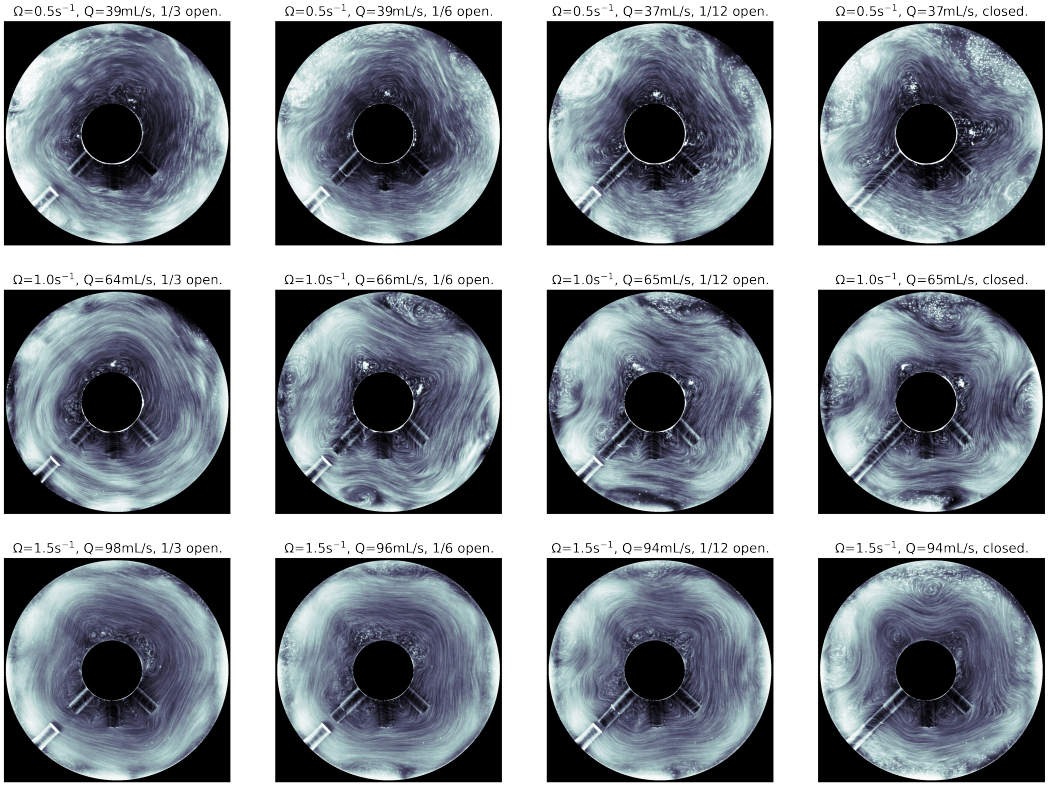

Figure 3. Streak photos developed from 4 seconds of footage. The imposed volume flux and rotation rate increases from the top row to the bottom; from left to right the columns show the 1/3, 1/6, and 1/12 open, and closed ridge cases.

4 Results and Discussions

4.1 Qualitative Description

All experiments exhibit a general cyclonic (clockwise) zonal flow throughout the annulus that is clearly influenced by the topographic ridges (Fig. 3). There is obvious radial structure to the zonal flow, with a single meandering mid-annulus jet that becomes increasingly apparent for larger rotation rates Ω and imposed volume fluxes Q. The effect of the topography is evidenced by radial disturbances in the flow as it crosses over the ridges, which are consequences of the conservation of potential vorticity. The three permanent inner ridges noticeably reduce the zonal flow in the inner third of the annulus. Localised intermittent eddying recirculations occur in the regions between the permanent ridges. Ubiquitous throughout the annulus are small-scale transient eddies that appear to become more intense for larger rotation rates Ω and imposed volume fluxes Q. The overflow over the inner edge wall appears to be zonally-uniform, and there is no evidence of permanently stagnant regions throughout the domain.

The mid-annulus zonal jet intensifies with increased rotation rates Ω and imposed volume fluxes Q, and decreased ridge gaps. The jet exhibits distinct radial meanders that are most intense immediately after crossing the ridge, and gradually decaying downstream. The radial position of where the jet crosses the ridge is set by the location of the gap; in the closed ridge cases the jet extends the full width of the annulus and reaches the outer edge wall immediately after it crosses the ridge. The radial extent of the meanders increases as the ridge gap decreases; the flows with the 1/3 gap configurations are

characteristically zonal with very little in the way of meanders. The radial extent of the meanders also appear to decay with the zonal flow downstream of the topography. In some experiments with lower imposed volume fluxes Q and large gaps the jet meanders are no longer obvious by the time the zonal flow recirculates the annulus back to the topography; for larger imposed volume fluxes Q and small or no gaps, however, the meanders persist throughout the annulus. Cyclonic and anticyclonic eddying recirculations exist on the inner and outer flanks of the jet, respectively, and tending to correspond with the locations of the meander peaks and troughs[1], respectively.

In all experiments, the radial extent of the jet is larger than the ridge gap, and the width of the jet appears insensitive to the ridge configuration. That said, it is interesting to note that even though the small ridge gaps are far narrower than the jet, and the volume flux through these small gaps represent a small fraction of the total jet flux, the very existence of these narrow gaps determine the radial location of the jet. This suggests that even a narrow gap is of dynamical importance for the jet; not necessarily for providing substantial volume flux to the jet, but perhaps by offering an efficient means to balance bottom pressure gradients either side of the ridge.

In summary, these rotation rates, imposed volume fluxes, topographic configurations (including the sloping false floor), and the geometry of the annulus, provide an effective laboratory model for a meandering jet, in which the circulation and jet are particularly sensitive to the size of the ridge gap, with this sensitivity seeming to increase for larger rotation rates Ω and imposed volume fluxes Q.

4.2 Particle Image Velocity Measurements

The PIV diagnosed velocity fields are consistent with the qualitative observations (Fig. 4). The mean flow speeds are maximum near mid-annulus and immediately downstream of the ridge. The speeds are largest for the 1/3 open cases and tend to decrease as the ridge gap closes. Local maxima of mean speed occur in the trough regions where the depth of the jet is shallowest and the radius of the jet is minimum. The spatial scales of the mean speed features are zonally-elongated; these tend to occupy approximately a third of the annulus radius, with their zonal extent decreasing as the ridge gap narrows.

The time-mean–zonal-mean zonal velocity $\overline{u}$ exhibits distinct radial structure that has a clear maximum at mid-annulus (Fig. 5). The maximum $\overline{u}$ decreases as the ridge gap narrows; the sensitivity of $\overline{u}$ to the gap size appears to increase with rotation rate Ω and imposed volume flux Q. There is good agreement between the observed $\overline{u}$ and that predicted by Hide (1968) (Eqn. 10) for the outer regions of the annulus. This agreement tends to peak around mid-annulus, and reduce for smaller radii. The disagreement at small radii is because the Hide (1968) prediction is formulated without topography, such that the predicted zonal velocity tends to continue to increase towards smaller radius (e.g., consider a sink vortex), rather than slowing because of interaction with the inner ridges.

We extend the presentation of the zonal velocity analysis to include all 72 experiments by comparing the observed maximum $\overline{u}$ to that predicted at $r = 0.4\,\mathrm{m}$ (Fig. 6a), which serves as a proxy measure for the forcing strength. There is generally good agreement between the predicted and observed zonal velocities, especially for ridge configurations with larger gaps; for the narrow and closed gap configurations the predicted velocities are larger than that observed, which makes sense considering that the Hide (1968) prediction is formulated without topography. The observed maximum velocity is sen-

[1] where the peaks and troughs refer to where the radius of the jet is at a maximum and minimum, respectively

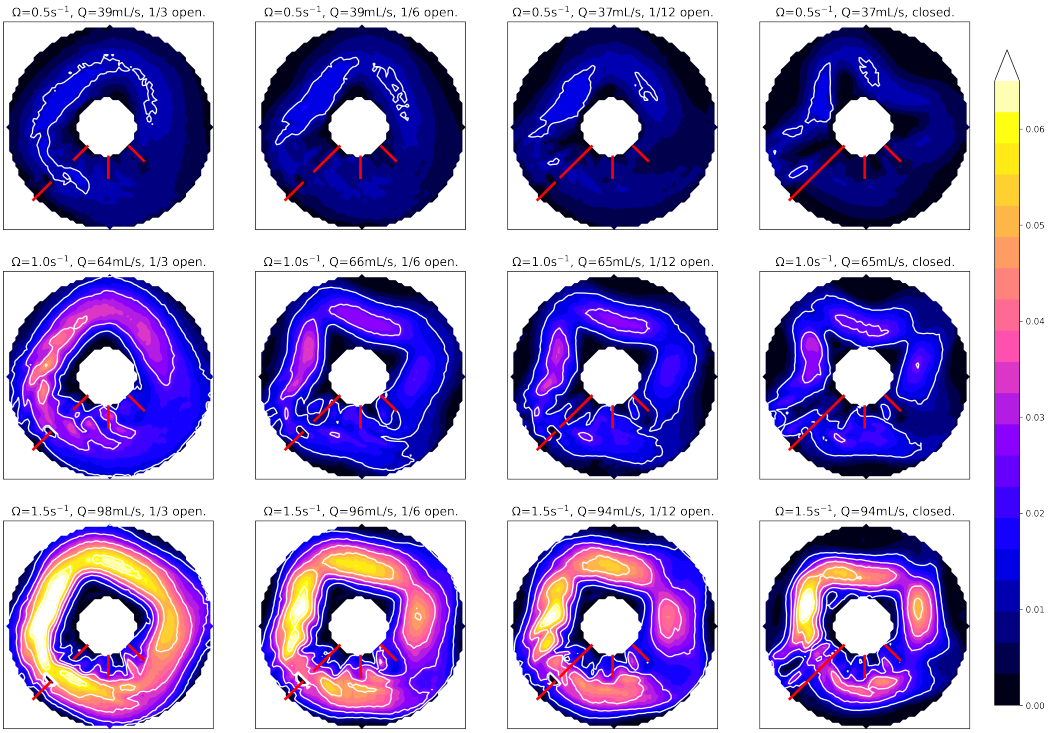

Figure 4. Average speed calculated from the PIV measurements for the same cases as shown in Figure 3. The imposed volume flux and rotation rate increases from the top row to the bottom; from left to right the columns show the 1/3, 1/6, and 1/12 open, and closed ridge cases. The white contours mark the 1.2 cm/s intervals up to 6.0 cm/s. The locations of the central ridge lines for each case are indicated in red.

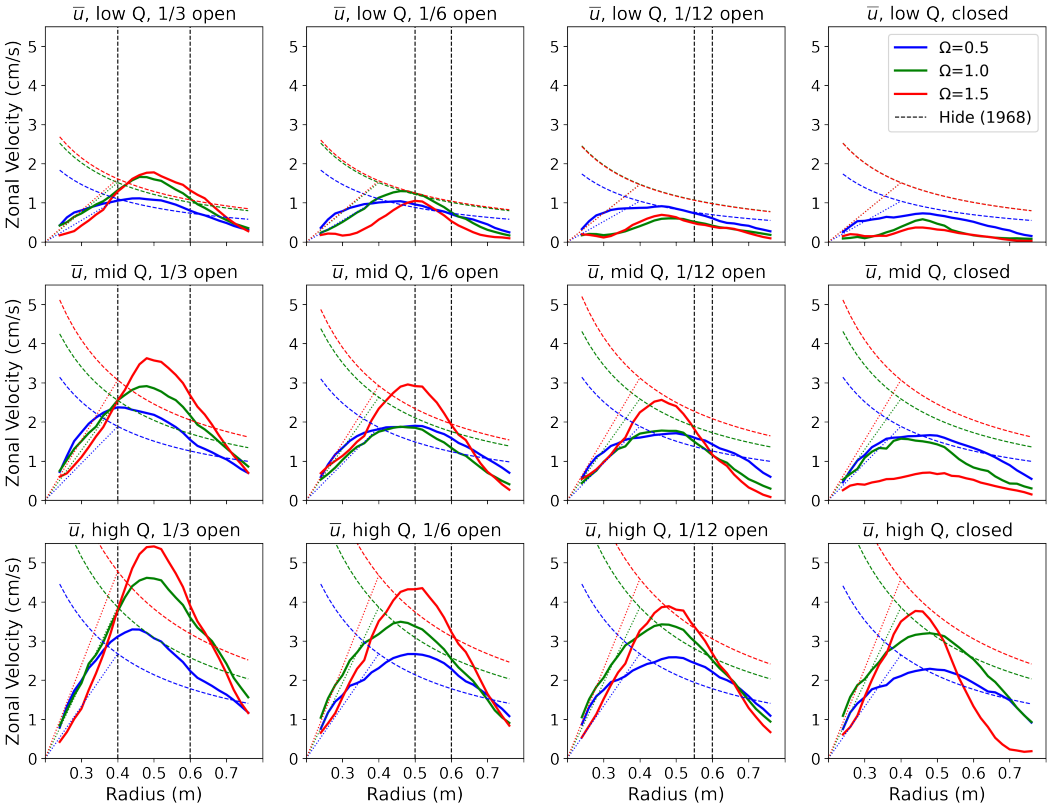

Figure 5. Time-mean–zonal-mean zonal velocity $\overline{u}$. The imposed volume flux Q increased from the top row to the bottom, and the extent of the ridge gap narrows from the left column to the right (as indicated by the vertical dashed black lines). Each figure shows the $\overline{u}$ for all three different rotation rates, with blue, green and red representing $\Omega = 0.5$, 1.0, 1.5, respectively. The dashed curves of the same colour represents the zonal velocities predicted by Hide (1968) (Eqn. 10). The dotted lines in each case is indicative of a linear reduction of zonal velocity wth radius from the predicted value at the outer edge of the permanent inner ridges ($r = 0.4\,\mathrm{m}$) to zero at the inner edge of the annulus ($r = 0.2\,\mathrm{m}$).

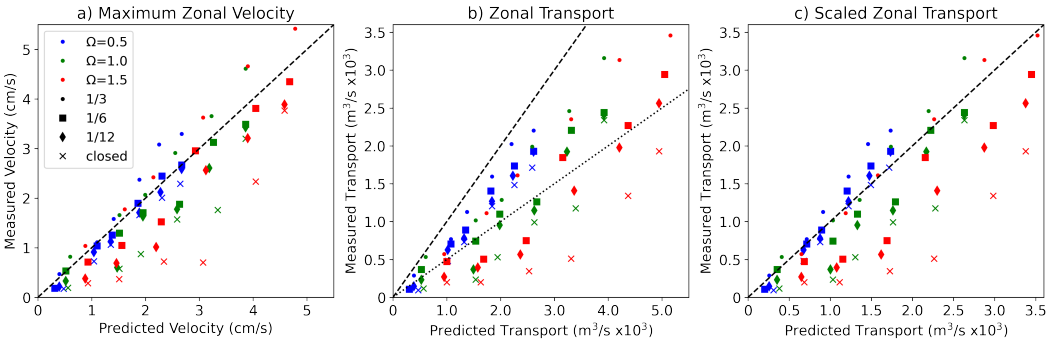

Figure 6. a) The predicted $\overline{u}$ at $r = 0.4\,\mathrm{m}$ compared to the observed maximum $\overline{u}$ for all 72 experiments; the colours represent the three different rotation rates, and the shapes reflect the ridge gaps. The slope of the dashed black line in all figures is 1:1. b) The predicted zonal transport compared to that observed; the slope of the dotted black line is 1:2. c) The predicted zonal transport if the zonal velocity linearly decreases to zero from $r = 0.4\,\mathrm{m}$ to $r = 0.2\,\mathrm{m}$ (dotted lines in Fig. 4) compared to that observed.

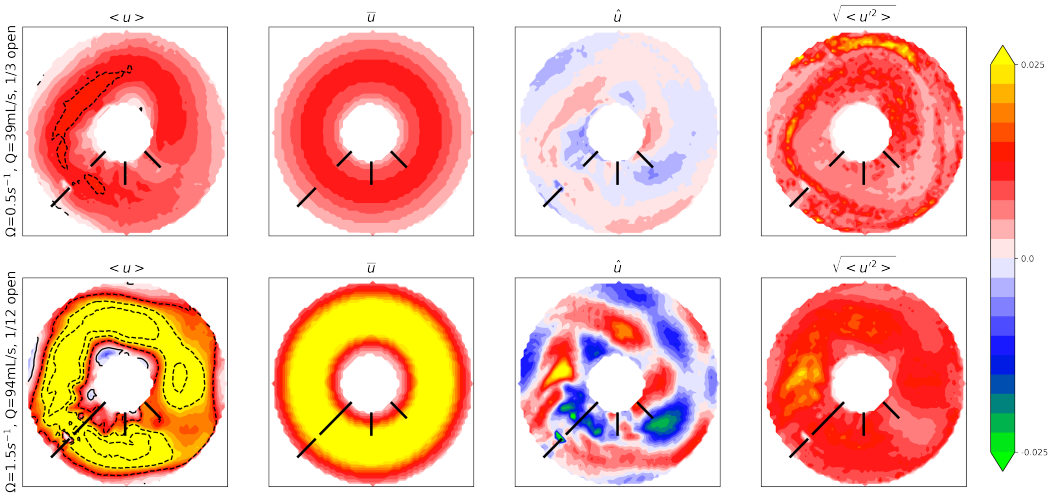

Figure 7. The time-mean of the total zonal velocity $\langle u \rangle$ decomposed into the time-mean–zonal-mean zonal velocity $\overline{u}$, standing meanders $\hat{u}$, and transient eddies $\sqrt{\langle u'^2 \rangle}$. The top row shows an experiment with low rotation rate, low imposed volume flux, and wide ridge gap, representative of a predominantly zonal flow state. The bottom row shows an experiment with high rotation rate, high imposed volume flux, and narrow ridge gap, representative of a predominantly meandering flow state. Both cases feature in Figures 3 and 4. Here positive zonal velocity is cyclonic/clockwise. The locations of the central ridge lines for each case are indicated in black.

sitive to the size of the ridge gap and is largest for the largest gap, and this sensitivity appears to be enhanced for larger rotation rates.

Radially integrating the time-mean–zonal-mean zonal velocities return the time-mean zonal transports for each experiment (Fig. 6b). In all experiments, the predicted zonal transport is larger than that observed, especially for larger rotation rates Ω, larger imposed volume fluxes Q and narrower ridge gaps. This over estimate of the zonal transport is likely because the Hide (1968) prediction of zonal velocity monotonically increases towards the inner edge of the annulus. Therefore, we calculate a scaled zonal transport with the velocity profiles that consist of the Hide (1968) prediction for $r > 0.4\,\mathrm{m}$, and linearly decrease with radius between $0.2 < r < 0.4\,\mathrm{m}$ to $\overline{u} = 0$ at the inner edge of the annulus (e.g., dotted lines in Fig. 5). Scaling the predicted zonal transports in this way returns much improved agreement with the observed transports, especially for the larger gap configurations (Fig. 6c). It is also important to note here that there is no evidence of eddy saturation effects observed here; increasing the imposed volume flux Q consistently results in an increased zonal transport.

The fact that the experiments with larger rotation rates appear to be more sensitive to the size of the gap is understood to be due to the combination of the fundamental dynamical lengthscale (Rossby deformation radius) being shorter for larger rotation rates, and that the radial gradient of the potential vorticity is larger. Both of these effects will operate to radially confine flow dynamics to narrower sections of the annulus; evidence of this can be seen in the streak photos and radial profiles of $\overline{u}$ (Figs. 3, 5). As such, the ratio of a given ridge gap relative to characteristic dynamical lengthscales of the flow increases for larger rotation rates, thereby making the flow more sensitive to changes in the ridge configuration.

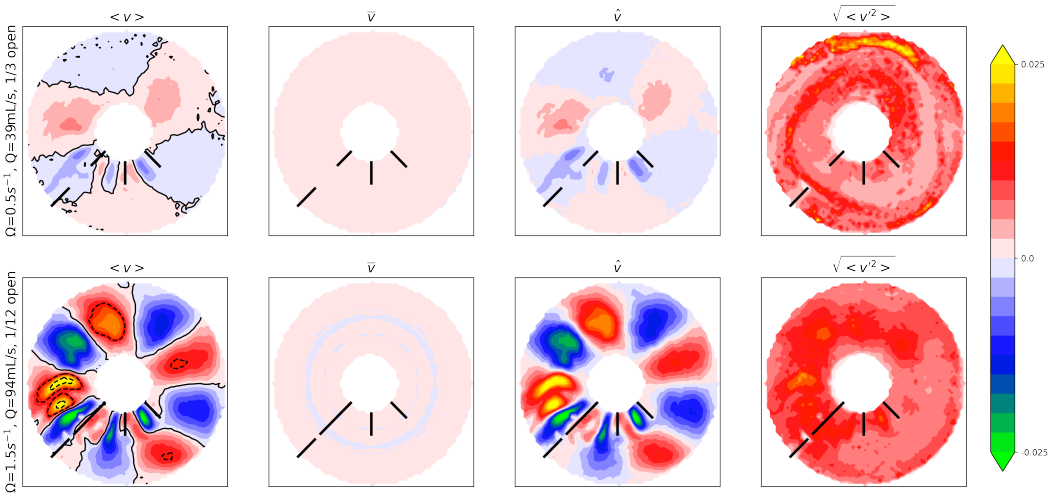

Figure 8. As for Figure 7, but for the time-mean of the radial velocity $\langle v \rangle$, decomposed into the time-mean–zonal-mean radial velocity $\overline{v}$, standing meanders $\hat{v}$, and transient eddies $\sqrt{\langle v'^2 \rangle}$. Here positive radial velocity is inwards. The locations of the central ridge lines for each case are indicated in black.

4.3 Decomposed Velocity Fields

Our qualitative observations and preliminary analyses of the mean speed and time-mean–zonal-mean zonal velocity fields clearly demonstrate that this configuration of the LRA facility and our experiment methodology produce a barotropic circulation with a single coherent zonal jet that has velocities and transports comparable to those predicted by existing theories. We now examine the velocity fields decomposed into their time-mean–zonal-mean flow, standing meanders and transient eddies as per Equation (13), noting that the transient eddy field is given by the square root of Equation (16). Here it is useful to focus on the comparison between the decomposed velocity fields of a case with a low rotation rate, low imposed volume flux, and wide ridge gap, to those of a case with high rotation rate, high imposed volume flux, and narrow ridge gap; these represent flow states that we refer to as being predominantly zonal and predominantly meandering, respectively.

The time-mean of the total zonal velocity is dominated by the time-mean–zonal-mean zonal velocity; in all experiments, regardless of whether the flow state is predominantly zonal or meandering, the total zonal velocity is well represented by the time-mean–zonal-mean zonal velocity (Fig. 7). For the predominantly zonal flow state, the standing meanders of the zonal velocity are of smaller magnitude than the time-mean–zonal-mean zonal velocity throughout the annulus, while the transient eddies are, in certain regions, larger than the time-mean–zonal-mean zonal velocity. There is relatively weak zonal or radial structure to the standing meanders. The distribution of the transient eddies generally follows that of the jet and exhibits a zonally-elongated and radially-confined structure.

For the predominantly meandering flow state, however, the standing meanders of the zonal velocity are, in certain regions, the same magnitude as the time-mean–zonal-mean zonal velocity. The standing meanders are of greater magnitude than the transient eddies throughout the annulus. There is substantially more structure to the standing meander distribution than that of the transient eddies, which is broad and not representative of the relatively narrower jet.

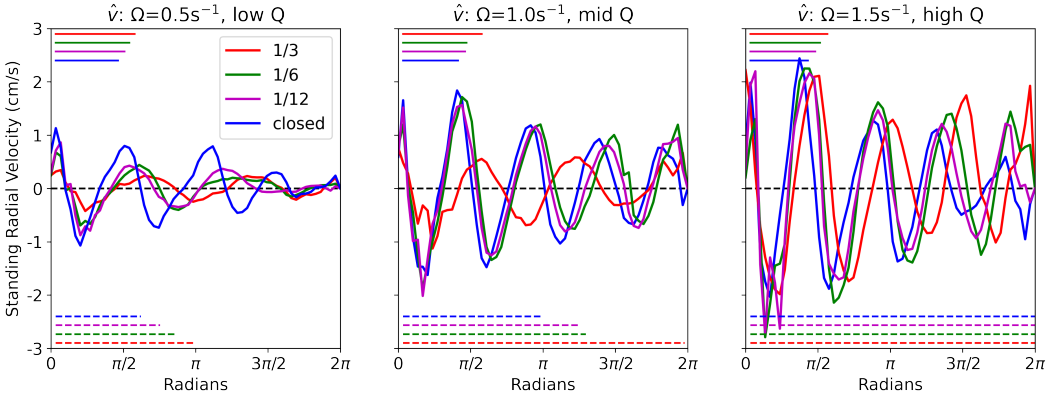

Figure 9. The radial standing meander velocity $\hat{v}$ at mid-annulus for low, mid- and high rotation rates and imposed volume fluxes (left to right). The abscissa is set such that the ridge is at 0. All four ridge configurations are shown for each case. The solid lines in the upper left of each figure represent the predicted Rossby wavelength in each case. The dashed lines in the lower left represent the angular distance travelled around the annulus by the jet in one Ekman dissipation timescale up to 2π.

Decomposing the radial velocity highlights the importance of the standing meander component (Fig. 8). In all experiments, the time-mean of the total radial velocity $\langle v \rangle$ is well represented by the standing meanders of the radial velocity $\hat{v}$, with the time-mean–zonal-mean radial velocity $\overline{v}$ being negligible. Note that the maximum imposed radial velocity given by Equation (5) is approximately 5×10^{-5} m/s, which for our methodology is indistinguishable from zero. The standing meanders of the radial velocity exhibit distinct zonal structure that alternate sign around the annulus. For the predominantly zonal flow state, the magnitude of the transient eddies of the radial velocity $\sqrt{\langle v'^2 \rangle}$ is greater than that of the radial standing meanders, and exhibit a similar distribution to that of the transient eddies zonal velocity $\sqrt{\langle u'^2 \rangle}$. In contrast, for the predominantly meandering flow state; the standing meanders are of greater magnitude than the transient eddies.

To further understand the meandering flow, we examine the zonal structure of the radial standing meander velocity $\hat{v}$ at mid-annulus (Fig. 9). The distinctive wave-like nature is obvious in all cases. The amplitude of the waves increases for increasing rotation rate and imposed volume flux. The wavelength of the meanders appears to be constant around the annulus, and are reminiscent of Rossby waves generated as the jet crosses the ridge. To verify whether this is the case, we calculate the wavelength λ_R predicted by (Rhines, 1975) for a standing Rossby wave in a background zonal flow U and meridional potential vorticity gradient β,

$$\lambda_R = 2\pi\sqrt{\frac{U}{\beta}}, \tag{20}$$

where the background zonal flow U is taken as the maximum time-mean–zonal-mean zonal velocity, and the meridional potential vorticity gradient is taken as the average gradient of potential vorticity across the annulus,

$$\beta = \frac{2\Omega\,(h_o - h_i)}{\overline{h}\,(r_o - r_i)}. \tag{21}$$

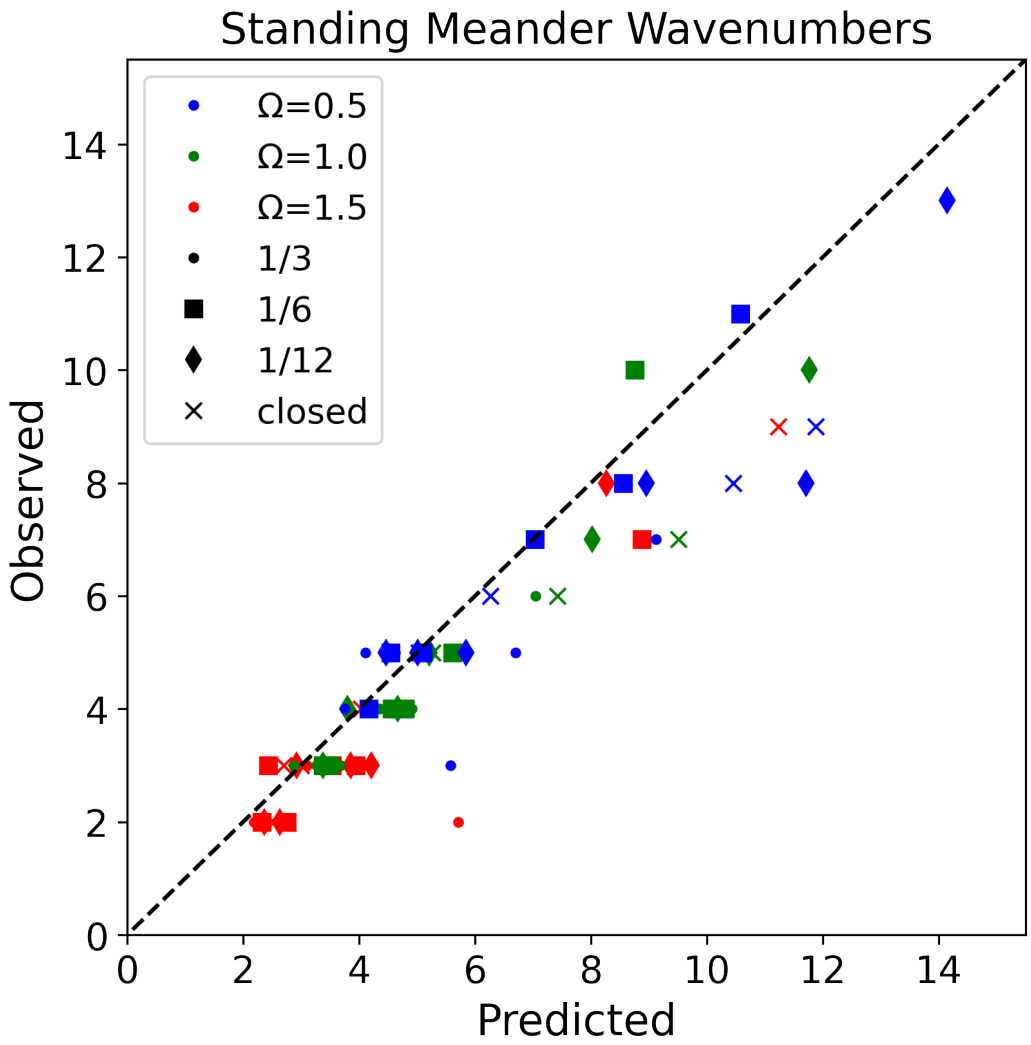

Figure 10. The predicted zonal wavenumber developed from the predicted Rossby wavelength λ_R compared with the observed zonal wavenumber obtained from the Fourier transform of the radial standing meander velocity $\hat{v}$ at mid-annulus.

For the experiments depicted in Figure 9, the predicted Rossby wavelength λ_R is included in the upper left panel; these exhibit good agreement with the radial standing meander velocity curves.

The comparison between the predicted Rossby wavelength and radial standing meander velocity curves can be extended by taking the Fourier transform of $\hat{v}$ to identify the peak zonal wavenumber for every experiment. These observed zonal wavenumber peaks are compared with the predicted zonal wavenumber developed from the predicted Rossby wavelength λ_R (Fig. 10). The close agreement between the observed and predicted wavenumbers is strong evidence that the standing meanders are indeed Rossby waves, and importantly, unlikely to be anything else.

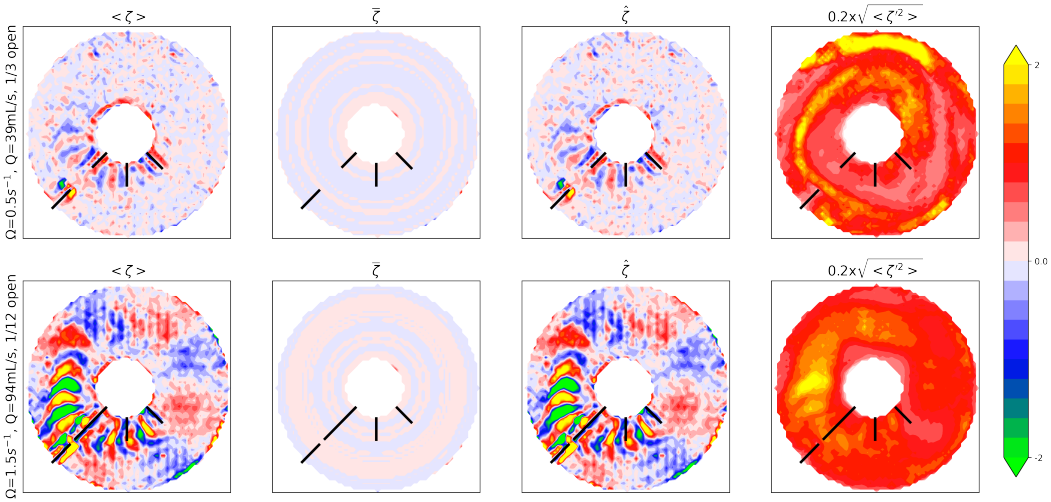

Figure 11. As for Figure 7, but for the time-mean of the vorticity $\langle\zeta\rangle$, decomposed into the time-mean–zonal-mean vorticity $\overline{\zeta}$, standing meanders $\hat{\zeta}$, and transient eddies $\sqrt{\langle\zeta'^2\rangle}$. Here positive vorticity is clockwise. Note that the transient eddy vorticity is scaled by 0.2. The locations of the central ridge lines for each case are indicated in black.

4.4 Radial Vorticity Fluxes

The distribution of the time-mean total vorticity $\langle\zeta\rangle$ is almost identical that of the standing meander vorticity $\hat{\zeta}$ (Fig. 11). Both of these fields exhibit structure with two zonal lengthscales; the smaller, and more intense, appears to be the lengthscale of the ridge, with the longer lengthscale being that of the Rossby waves. The time-mean–zonal-mean vorticity field is negligible. The magnitude of the transient eddy vorticity is substantially larger than that of the standing meander vorticity. For the predominantly zonal flow state the transient eddy vorticity is zonally-elongated and radially-confined, while for the predominantly meandering state it is relatively broader and less coherent.

From the product of the radial velocity and vorticity we calculate the total radial vorticity flux, and decompose it into its time-mean–zonal-mean, standing meanders, and transient eddy components (Eqn. 19; Fig. 12). The time-mean–zonal-mean radial vorticity flux is negligible in all experiments, leaving the time-mean of the total radial vorticity flux to be performed by the standing meanders and transient eddies. In the predominantly zonal flow state, the transient eddy radial vorticity flux is the dominant contributor to the total radial vorticity flux. For the predominantly meandering flow state, however, the standing meander contribution is dominant.

The relative contributions of the radial vorticity fluxes can be compared by taking their zonal averages and plotting by radius (Fig. 13). In all experiments, the total radial vorticity flux shows reasonable agreement with the estimated imposed radial vorticity flux for radii larger than the extent of the inner ridges (Eqn. 7), and especially at the outer edge of the inner ridges ($r = 0.4\,\mathrm{m}$). For low rotation rates, low imposed volume fluxes, and wide ridge gaps, the radial distribution of the total radial vorticity flux is dominated by the transient eddy contribution. As the experiment configurations tend to larger rotation rates, larger imposed volume fluxes, and narrower ridge gaps, the standing meander radial vorticity flux becomes the dominant contribution. That said, the transient eddy contribution of these predominantly meandering flow states is not negligible.

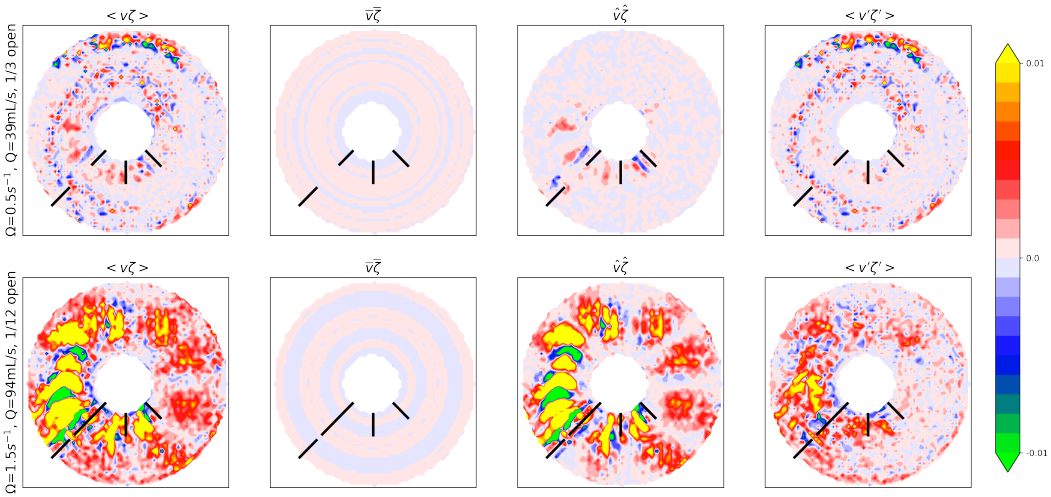

Figure 12. As for Figure 7, but for the time-mean of the radial vorticity flux $\langle v\zeta \rangle$, decomposed into the time-mean–zonal-mean radial vorticity flux $\overline{v}\overline{\zeta}$, standing meander radial vorticity flux $\hat{v}\hat{\zeta}$, and transient eddy radial vorticity flux $\langle v'\zeta' \rangle$. Here positive vorticity flux is inwards. The locations of the central ridge lines for each case are indicated in black.

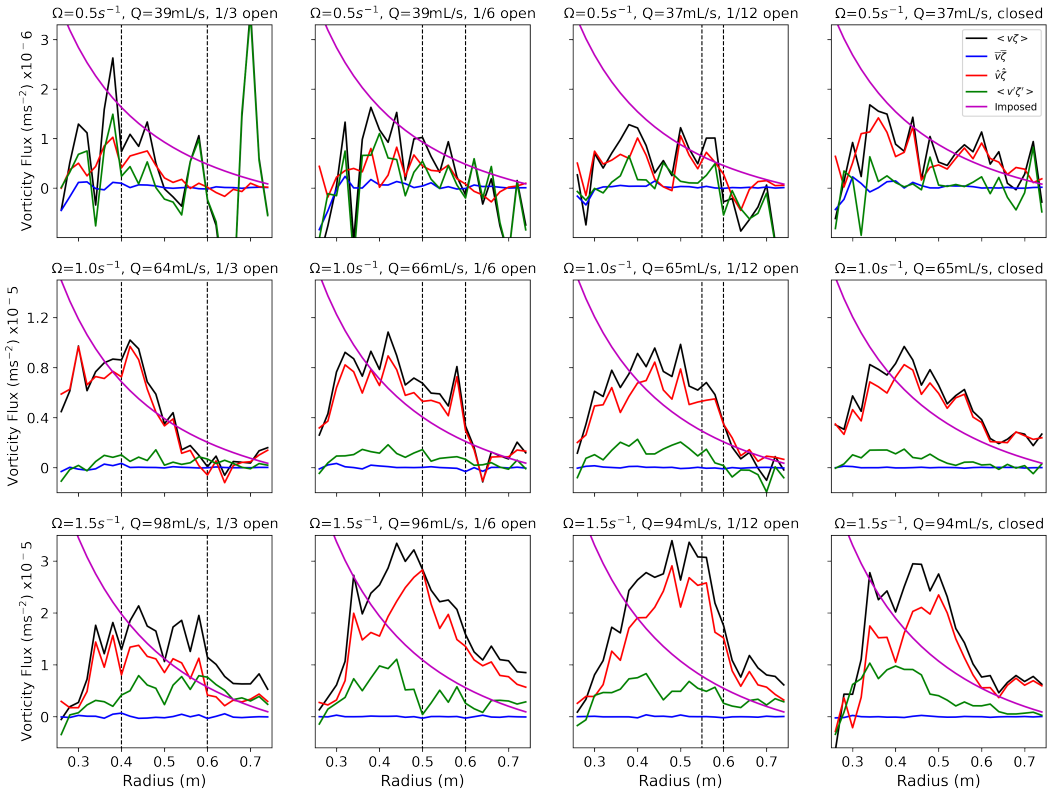

Figure 13. Radial distributions of the zonally-averaged time-mean total radial vorticity flux $\langle v\zeta \rangle$ (black), time-mean–zonal-mean radial vorticity flux $\overline{v}\overline{\zeta}$ (blue), standing meander radial vorticity flux $\hat{v}\hat{\zeta}$ (red), and transient eddy radial vorticity flux $\langle v'\zeta' \rangle$ (green). The magenta curves show estimates of the imposed radial vorticity flux (Eqn. 7); these estimates do not account for the influence of the ridges, and likely to be invalid for $r < 0.4\,\mathrm{m}$. The vertical dashed lines indicate the radial extent of the ridge gaps. Here positive vorticity flux is inwards.

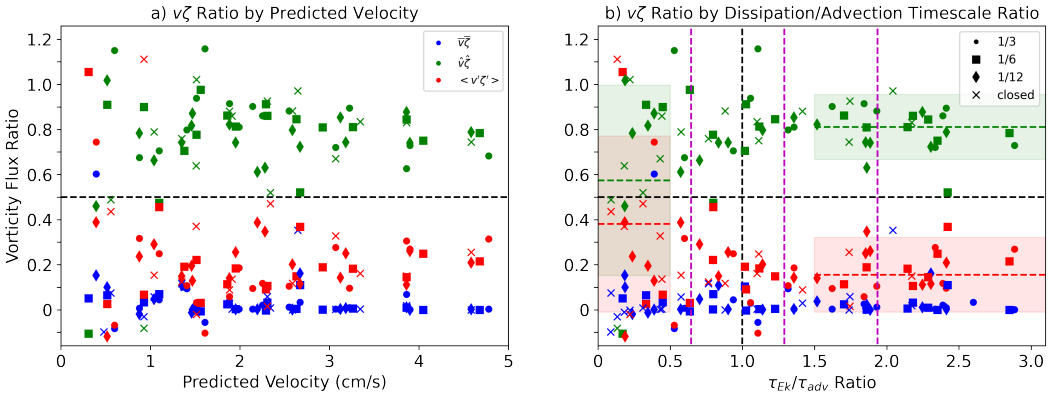

Figure 14. Ratios of the zonally-averaged time-mean–zonal-mean radial vorticity flux $\overline{v}\overline{\zeta}$ (blue), standing meander radial vorticity flux $\hat{v}\hat{\zeta}$ (red), and transient eddy radial vorticity flux $\langle v'\zeta' \rangle$ (green) to the time-mean total radial vorticity flux $\langle v\zeta \rangle$. The black horizontal dashed lines represent the 0.5 level. a) The radial vorticity flux ratios are calculated for all experiments and plotted by their predicted zonal velocity at $r = 0.4\,\mathrm{m}$ (as per Fig. 6a). b) The ratios are plotted by their dissipation-to-advection timescale ratio. For reference, the 1:1 timescale ratio is shown (black vertical dashed line), along with the timescale ratios representative of the Northern Hemisphere jet stream for speeds of 100, 200 and 300km/h (magenta dashed lines, with speeds increasing to the right). The average vorticity flux ratios of the standing meander and transient eddy contributions are included for dissipation-to-advection timescale ratios of less than 0.5 and greater than 1.5, with the shading indicative of the respective standard deviation.

We can take the analysis further by comparing the full annulus average of the ratios of the three radial vorticity flux components to the total radial vorticity flux. Note that for each experiment these three ratios sum to 1, but each component is not necessarily positive, such that individual ratios can be greater than 1 and/or less than zero. We first plot these ratios with respect to the predicted zonal velocity at $r = 0.4\,\mathrm{m}$ (Eqn. 10), which is a proxy for the strength of the forcing conditions provided by the imposed volume flux Q and rotation rate Ω (Fig. 14a). As the strength of the forcing increases, indicated by an increased $\overline{u}$, the vorticity flux ratios of the standing meander and transient eddy contributions tend to become distinct, with the standing meander contribution becoming dominant.

Dynamical context can be given to the forcing condition proxy by considering the timescales involved. Specifically, the Ekman dissipation timescale τ_{Ek} (Eqn. 9) describes the characteristic timescale in which Ekman processes damp unbalanced flows, such as the Rossby wave meanders. This damping of the meanders is evident in the distributions of velocities, and in particular, in the decay of standing meander velocity amplitudes downstream of the ridge in Figure 9. Furthermore, the dashed lines in Figure 9 are indicative of the distance travelled by the jet in one Ekman dissipation timescale; when the dashed line extends to 2π, it indicates that jet is able to circuit the annulus faster than Ekman processes can dissipate variability. In other words, the jet advection timescale τ_{adv} (Eqn. 11) is shorter than the Ekman dissipation timescale. The ratio of the the dissipation and advection timescale provides a useful metric to classify when the flow disturbances generated by the jet-topography interaction are able to survive a complete circuit of the annulus, and be able to be reinforced through further topographic interactions. Note that there is no evidence that this phenomenon requires the meanders to reach the ridge with a particular Rossby waves phase or other resonance criterion.

Figure 14b plots the radial vorticity flux ratios by the dissipation-to-advection timescale ratio. There is clear distinction between the timescale ratios less than and greater than unity; for configurations with timescales less than one, which coincide with the predominantly zonal flow states, the radial vorticity flux is achieved by both standing meanders and transient eddies. Indeed, for experiments with $\tau_{Ek}/\tau_{adv} < 0.5$, the average radial vorticity flux ratio for the standing meander and transient eddy contributions are 57±42% and 38±39%, respectively, and thus statistically similar. For dissipation-to-advection timescale ratios greater than 1.5, however, which represents the predominantly meandering flow states, 81±14% of the radial vorticity flux is performed by the standing meanders, with 15±16% by transient eddies, and clear separation between their statistical distributions.

5 Geophysical Implications

The laboratory experiments with this configuration of the LRA have produced circulations with a coherent zonal jet punctuated with Rossby waves and two distinct flow regimes; predominantly zonal flow, and predominantly meandering flow. While the flow regime of a given experiment may be qualitatively obvious, we find it can be quantified by the ratio of the Ekman dissipation and zonal advection timescales. That is, if variability arising from flow-topography interaction at the ridge is able to be advected completely around the annulus and back to the ridge before it is dissipated, then this variability is able to be reinforced and amplified by subsequent topographic interactions, leading to predominantly meandering flow conditions. For predominantly zonal flows, the transient eddies perform the majority of the radial vorticity flux associated with the imposed radial volume flux Q. For predominantly meandering flows, the standing meanders accommodate 81±14% of the total radial vorticity flux, with the transient eddies contributing the rest.

We can offer geophysical context to the findings of the laboratory experiments by estimating the Ekman dissipation and zonal advection timescale ratios for the Northern Hemisphere jet streams, which influences the weather for more than half of the world's population. For this we consider a 10 km thick atmosphere at 50°N with an eddy viscosity of $5\,\mathrm{m}^2/\mathrm{s}$, which are typical values (e.g., Holton & Hakim, 2013). Figure 14b includes 3 dashed magenta vertical lines that indicate the dissipation-to-advection timescale ratios for zonal wind speeds of 100, 200 and 300 km/h (left to right). For 100 km/h zonal wind speeds, the dissipation timescale is faster than the advection timescale, indicative of predominantly zonal flows with transient eddies performing meridional fluxes of tracer, i.e., variable, synoptic weather conditions. For zonal wind speeds greater than 200 km/h, however, the dissipation-to-advection timescale ratio is larger than one, suggesting the system will be in the predominantly meandering flow regime and prone to persistent extreme weather conditions. For reference, from Equation 20, the zonal wavenumbers of standing Rossby waves at 50°N for zonal wind speeds of 100, 200 and 300 km/h are 3, 2 and 2, respectively.

Based on the criteria of (Woollings et al., 2018), many of the circulations in the experiments described here would be classified as a blocked flow regime, albeit locally blocked. Some of our circulations represent what is perhaps the simplest example of blocked flows: stationary ridges in large-amplitude Rossby waves. These stationary ridges can occur in isolation for a single Rossby wave and tend to bring anticyclonic, high pressure conditions to higher latitudes, leading to persistent warm weather that can last several days. In terms of our experiments, the stationary ridge blocked regime is reminiscent of cases where Rossby waves are excited but dissipate locally; this includes several cases of what we consider as predominantly zonal flow conditions, noting that our definition describes the global state. It is also evident that the local dynamics in regions influenced by the stationary Rossby waves exhibit a greater dependence on the standing meander component of the flow, and less on the transient eddies. Considering the low-wavenumbers typical of stationary Rossby waves, our findings imply that an isolated stationary ridge block

can have a continental-scale influence on weather conditions, whereby the local meridional transport of tracer is performed by jet meanders rather than synoptic variability.

Another example of a blocked flow regime is known as quasi-resonant amplification (QRA), which arises from the trapping of planetary waves in latitudinal waveguides, thereby providing a mechanism for resonance and a subsequent amplification (e.g., Petoukhov et al., 2013; Screen & Simmonds, 2014; Mann et al., 2018). The specifics of the QRA state, such as its dominant wavenumber, depend on the details of the latitudinal waveguide, and the wave forcing and damping; for the Northern Hemisphere, the topography and atmospheric conditions favour the QRA of wavenumbers in the synoptic range (6–8). The QRA events are circumpolar, leading to extreme persistent weather conditions occurring concurrently in multiple locations. In terms of our experiments, where the laboratory analog of the latitudinal waveguide is due to the radially-dependent fluid depth and zonal flow speed, the predominantly meandering flow state is equivalent to the QRA blocked regime. In this state, the jet meanders perform the bulk of the global meridional tracer transport.

A prominent aspect of climate change is Arctic amplification, which refers to the fact that higher northern latitudes are tending to warm faster than lower latitudes, thereby reducing the meridional gradient of air temperature. (Note, that an equivalent Antarctic amplification is predicted to occur in the Southern Hemisphere as well, but to a lesser extent.) Given that the zonal wind speed depends on this meridional gradient of air temperature, Arctic amplification will likely to reduce these wind speeds. It has been suggested that slower zonal winds will occur in conjunction with enhanced meridional meandering and an increased occurrence of atmospheric blocks (e.g., Francis & Vavrus, 2012). This hypothesis disagrees with projections from climate, atmospheric and idealised models, which indicate Arctic amplification leads to a decline in blocking events and a decrease in Rossby wave amplitudes (e.g., Barnes et al., 2011; Dunn-Sigouin & Son, 2013; Hassanzedeh et al., 2014; Kennedy et al., 2016). Our analysis here indeed suggests that weaker forcing conditions (lower rotation rate Ω and imposed volume flux Q) lead to a predominantly zonal flow regime in which transient eddies perform the bulk of the meridional tracer transport.

6 Conclusions

We investigated the dynamics of meandering zonal jets in the laboratory using experiments in the Large Rotating Annulus. The configuration of the small-scale topography determines the radial position and phase of the zonal jet at the location of the ridge, following which the jet is free to evolve downstream around the annulus. This methodology permits the internal dynamics of the system determine the zonal structure of the flow, rather than the geometry of the topography, the thereby exciting a much wider range of zonal wavenumbers as compared with previous laboratory experiments (e.g., Weeks et al., 1997; Tian et al., 2001). The interaction between the flow and topography generates Rossby waves, which can become stationary when their propagation speed matches that of the zonal jet, reminiscent of an atmospheric blocked flow state.

We find the circulations can be classified into two distinct regimes; predominantly zonal, and predominantly meandering flow. In the predominantly zonal flow regime, disturbances generated by the flow-topography interaction are dissipated faster than the time taken to be advected around the annulus. Stationary Rossby waves can be present immediately downstream of the topography, leading to a locally blocked flow state, but their amplitude decays before circuiting the annulus. Transient eddies perform the bulk of the radial transport of tracer, except in the vicinity of stationary Rossby waves. Predominantly meandering flows, however, occur when disturbances arising from the flow-topography interaction are able to be reinforced and amplified upon subsequent encounters with the topography. In this state, which resembles the atmospheric quasi-resonant

amplification blocked regime, the standing meanders of the jet are responsible for 81±14% of the radial transport of tracer, with transient eddies performing the rest. Our findings suggest that the decreasing zonal wind speed associated with Arctic amplification will lead to predominantly zonal flow conditions, thereby localising and/or reducing the occurrences of atmospheric blocking events caused by the jet streams.

Acknowledgments

We are grateful to Andy Hogg, Callum Shakespeare, Navid Constantinou, and Josué Martinez Moreno for their insightful discussions and helpful comments. We wish to thank Angus Rummery, Tony Beasley and Gordon Scott for the construction of the apparatus and laboratory assistance. Upon acceptance, the velocity data generated by the PIV analysis will be published at Zenodo and the digital object identifier (doi) will be quoted here.

References

Aguiar, A., Read, P., Wordsworth, R., Salter, T., & Yamazaki, Y. (2010). A laboratory model of Saturn's north polar hexagon. *Icarus*, *206*, 755–763. doi: 10.1016/j.icarus.2009.10.022

Barnes, E., Slingo, J., & Woollings, T. (2011). A methodology for the comparison of blocking climatologies across indices, models and climate scenarios. *Climate Dynamics*, *38*, 2467–2481. doi: 10.1007/s00382-011-1243-6

Cabanes, S., Aurnou, J., Favier, B., & Le Bars, M. (2017). A laboratory model for deep-seated jets on the gas giants. *Nature Physics*, *13*, 387–390. doi: 10.1038/NPHYS4001

Dunn-Sigouin, E., & Son, S.-W. (2013). Northern Hemisphere blocking frequency and duration in the CMIP5 models. *Journal of Geophysical Research: Atmosphere*, *118*, 1179–1188. doi: 10.1002/jgrd.50143

Francis, J., & Vavrus, S. (2012). Evidence linking Arctic amplification to extreme weather in mid-latitudes. *Geophysical Research Letters*, *39*, L06801. doi: 10.1029/2012GL051000

Früh, W.-G., & Read, P. (1999). Experiments on a barotropic rotating shear layer. part 1. instability and steady vortices. *Journal of Fluid Mechanics*, *383*, 143–171. doi: 10.1017/S0022112098003930

Galperin, B., & Read, P. (2019). Zonal Jets: Phenomenology, Genesis, and Physics. Cambridge University Press. doi: 10.1017/9781107358225

Hassanzedeh, P., Kuang, Z., & Farrell, B. (2014). Responses of midlatitude blocks and wave amplitude to changes in the meridional temperature gradient in an idealized dry GCM. *Geophysical Research Letters*, *41*, 5223–5232. doi: 10.1002/2014GL060764

Hide, R. (1968). On source-sink flows in a rotating fluid. *Journal of Fluid Mechanics*, *32*, 737–764. doi: 10.1017/S002211206800100X

Hide, R., & Titman, C. (1967). Detached shear layers in a rotating fluid. *Journal of Fluid Mechanics*, *29*, 39–60. doi: 10.1017/S002211206700062X

Holton, J., & Hakim, G. (2013). An Introduction to Dynamic Meteorology, 5th ed. Academic Press. doi: 10.1016/C2009-0-63394-8

Hoskins, B., McIntyre, M., & Robertson, A. (1985). On the use and significance of isentropic potential vorticity maps. *Quarterly Journal of the Royal Meteorological Society*, *111*, 877–946. doi: 10.1002/qj.49711147002

Hoskins, B., & Woollings, T. (2015). Persistent extratropical regional and climate extremes. *Current Climate Change Reports*, *1*, 115–124. doi: 10.1007/s40641-015-0020-8

Kennedy, D., Parker, T., Woollings, T., Harvey, B., & Shaffrey, L. (2016). The response of high-impact blocking weather systems to climate change. *Geophysical*

Research Letters, *43*, 7250–7258. doi: 10.1002/2016GL069725

Lemasquerier, D., Favier, B., & Le Bars, M. (2021). Zonal jets at the laboratory scale: hysteresis and Rossby waves resonance. *Journal of Fluid Mechanics*, *910*, A18. doi: 10.1017/jfm.2020.1000

Lu, J., Chen, G., Leung, L., Burrows, D., Yang, Q., Sakaguchi, K., & Hagos, S. (2015). Towards the dynamical convergence on the Jet Stream in Aquaplanet AGCMs. *Journal of Climate*, *28*, 6763–6782. doi: 10.1175/JCLI-D-14-00761.1

Mann, M., Rahmstorf, S., Kornhuber, K., Steinman, B., Miller, S., Petri, S., & Coumou, D. (2018). Projected changes in persistent extreme summer weather events: The role of quasi-resonant amplification. *Science Advances*, *4*, eaat3272. doi: 10.1126/sciadv.aat3272

Marcus, P., & Lee, C. (1998). A model for eastward and westward jets in laboratory experiments and planetary atmospheres. *Physics of Fluids*, *10*, 1474–1489. doi: 10.1063/1.869668

Niino, H., & Masawa, N. (1984). An experimental and theoretical study of barotropic instability. *Journal of Atmospheric Sciences*, *41*, 1992–2011. doi: 10.1175/1520-0469(1984)041⟨1992:AEATSO⟩2.0.CO;2

Petoukhov, V., Rahmstorf, S., Petri, S., & Schellnhuber, H. (2013). Quasiresonant amplification of planetary waves and recent Northern Hemisphere weather extremes. *Proceedings of the National Academy of Sciences*, *110*, 5336–5341. doi: 10.1073/pnas.1222000110

Read, P. (2019). Zonal jet flows in the laboratory: An introduction. In B. Galperin & P. Read (Eds.), *Zonal Jets: Phenomenology, Genesis, and Physics* (pp. 119–134). Cambridge University Press. doi: 10.1017/9781107358225.006

Read, P., Kennedy, D., Lewis, N., Scolan, H., Tabataba-Vakili, F., Wang, Y., ... Young, R. (2020). Baroclinic and barotropic instabilities in planetary atmospheres: energetics, equilibration and adjustment. *Nonlinear Processes in Geophysics*, *27*, 147–173. doi: 10.5194/npg-27-147-2020

Rhines, P. (1975). Waves and turbulence on a beta-plane. *Journal of Fluid Mechanics*, *69*, 417–443. doi: 10.1017/S0022112075001504

Screen, J., & Simmonds, I. (2014). Amplified mid-latitude planetary waves favour particular regional weather extremes. *Nature Climate Change*, *4*, 704–709. doi: 10.1038/NCLIMATE2271

Solomon, T., Holloway, W., & Swinney, H. (1993). Shear flow instabilities and Rossby waves in barotropic flow in a rotating annulus. *Physics of Fluids A: Fluid Dynamics*, *5*, 1971–1982. doi: 10.1063/1.858824

Sommeria, J., Meyers, S., & Swinney, H. (1989). Laboratory model of a planetary eastward jet. *Nature*, *337*, 58–61. doi: 10.1038/337058a0

Tian, Y., Weeks, E., Ide, K., Urbach, J., Baroud, C., Ghil, M., & Swinney, H. (2001). Experimental and numerical studies of an eastward jet over topography. *Journal of Fluid Mechanics*, *438*, 129–157. doi: 10.1017/S0022112001004372

Weeks, E., Tian, Y., Urbach, J., Ide, K., Swinney, H., & Ghil, M. (1997). Transitions between blocked and zonal flows in a rotating annulus with topography. *Science*, *278*, 1598–1601. doi: 10.1126/science.278.5343.1598

Woollings, T., Barriopedro, D., Methven, J., Son, S.-W., Martius, O., Harvey, B., ... Seneviratne, S. (2018). Blocking and its response to climate change. *Current Climate Change Reports*, *4*, 287–300. doi: 10.1007/s40641-018-0108-z